



ISTITUTO NAZIONALE DI RICERCA METROLOGICA Repository Istituzionale

Nanodiamond-Quantum Sensors Reveal Temperature Variation Associated to Hippocampal Neurons Firing

Original

Nanodiamond-Quantum Sensors Reveal Temperature Variation Associated to Hippocampal Neurons Firing / Petrini, Giulia; Tomagra, Giulia; Bernardi, Ettore; Moreva, Ekaterina; Traina, Paolo; Marcantoni, Andrea; Picollo, Federico; Kvaková, Klaudia; Cígler, Petr; Degiovanni, Ivo Pietro; Carabelli, Valentina; Genovese, Marco. - In: ADVANCED SCIENCE. - ISSN 2198-3844. - 9:28(2022), pp. 1-11. [10.1002/advs.202202014]

Availability:

This version is available at: 11696/76179 since: 2023-02-28T14:23:46Z

Publisher:

WILEY

Published

DOI:10.1002/advs.202202014

Terms of use:

This article is made available under terms and conditions as specified in the corresponding bibliographic description in the repository

Publisher copyright

(Article begins on next page)

Nanodiamond–Quantum Sensors Reveal Temperature Variation Associated to Hippocampal Neurons Firing

Giulia Petrini, Giulia Tomagra, Ettore Bernardi, Ekaterina Moreva, Paolo Traina, Andrea Marcantoni, Federico Picollo, Klaudia Kvaková, Petr Cígler, Ivo Pietro Degiovanni, Valentina Carabelli, and Marco Genovese*

Temperature is one of the most relevant parameters for the regulation of intracellular processes. Measuring localized subcellular temperature gradients is fundamental for a deeper understanding of cell function, such as the genesis of action potentials, and cell metabolism. Notwithstanding several proposed techniques, at the moment detection of temperature fluctuations at the subcellular level still represents an ongoing challenge. Here, for the first time, temperature variations (1 °C) associated with potentiation and inhibition of neuronal firing is detected, by exploiting a nanoscale thermometer based on optically detected magnetic resonance in nanodiamonds. The results demonstrate that nitrogen-vacancy centers in nanodiamonds provide a tool for assessing various levels of neuronal spiking activity, since they are suitable for monitoring different temperature variations, respectively, associated with the spontaneous firing of hippocampal neurons, the disinhibition of GABAergic transmission and the silencing of the network. Conjugated with the high sensitivity of this technique (in perspective sensitive to < 0.1 °C variations), nanodiamonds pave the way to a systematic study of the generation of localized temperature gradients under physiological and pathological conditions. Furthermore, they prompt further studies explaining in detail the physiological mechanism originating this effect.

1. Introduction

On the one side, temperature regulates the speed of ion channel opening,^[1] the pattern activity of a firing neuron,^[2] and the vesicular dynamics at the presynaptic terminal,^[3] on the other side, intracellular temperature is affected by a variety of biochemical reactions occurring during cell activity. Pioneering findings dating back to the late 70s,^[4,5] associated temperature increases to the impulse propagation in nonmyelinated fibers of the olfactory nerve and, more recently, a theoretical explanation about the heat production and absorption by neurons during nervous conduction has been formulated.^[6] Intracellular temperature variations have been probed to detect the phases of cell-cycle division^[7] and the mitochondrial activity.^[8] In the brain, temperature fluctuations are likely associated with changes in neuronal functions such as the genesis of action potentials, secretion at the level of synaptic terminals, or transmembrane ion

G. Petrini, E. Bernardi, E. Moreva, P. Traina, I. P. Degiovanni, M. Genovese
Istituto Nazionale di Ricerca Metrologica
Strada delle cacce 91, Torino 10135, Italy
E-mail: m.genovese@inrim.it

G. Petrini, F. Picollo
Physics Department, University of Torino
via P. Giuria 1, Torino 10125, Italy


G. Petrini, G. Tomagra, A. Marcantoni, V. Carabelli
Department of Drug and Science Technology, University of Torino
Corso Raffaello 30, Torino 10125, Italy

G. Tomagra, A. Marcantoni, V. Carabelli
NIS Inter-departmental Centre
via G. Quarello 15, Torino 10135, Italy

F. Picollo, I. P. Degiovanni, M. Genovese
Istituto Nazionale di Fisica Nucleare (INFN) Sez. Torino
via P. Giuria 1, Torino 10125, Italy

K. Kvaková
Institute of Organic Chemistry and Biochemistry of the Czech Academy of Sciences
Flemingovo nám. 2, Prague 6 166 10, Czechia

K. Kvaková, P. Cígler
Institute of Medical Biochemistry and Laboratory Diagnostics
First Faculty of Medicine
Charles University
Katerinska 1660/32, Prague 2 121 08, Czechia

 The ORCID identification number(s) for the author(s) of this article can be found under <https://doi.org/10.1002/advs.202202014>

© 2022 The Authors. Advanced Science published by Wiley-VCH GmbH. This is an open access article under the terms of the Creative Commons Attribution License, which permits use, distribution and reproduction in any medium, provided the original work is properly cited.

DOI: 10.1002/advs.202202014

transports.^[9–11] Variation of intracellular temperature is also related to changes in cell metabolism, as observed through positron emission tomography and functional magnetic resonance imaging (fMRI).^[12]

Besides its fundamental role in cell physiology, the temperature may be altered under pathological conditions, such as in cancerous cells,^[13] which display higher metabolic activity, in neurodegeneration, such as Parkinson's or Alzheimer's diseases, where the process of abnormal protein aggregation is temperature-dependent,^[14] or during the onset of *malignant hyperthermia*, a pathology that causes rapid temperature increases following excessive muscle contraction.^[15]

Furthermore, an increase in local temperature, up to a few Celsius degrees, has been detected as triggered by laser heating,^[16] calcium stress,^[17] direct electric stimulation,^[18] or using drugs that increase the heat produced during cellular respiration.^[16,18,19] These results, in particular the ones related to the highest temperature variations, stimulated a debate since the power needed to justify this temperature growth has been calculated to exceed a few orders of magnitude what is expected by thermodynamic considerations in a model where thermal diffusion is characterized by conductive regime.^[20] Nonetheless, other authors^[21,22] suggested that, by taking into account the inhomogeneity of the cells, this gap can be strongly reduced.

However, detection of temperature fluctuations at the sub-cellular level still represents an ongoing challenge and several intracellular thermometry techniques are reported in the literature, ranging from fluorescent molecular thermometers,^[23] quantum dots,^[24] or rare-earth nanoparticles.^[25] Compared to the above-mentioned methods, nanodiamonds (ND) show a better biocompatibility,^[26,27] insensitivity to biological environment,^[28] more stable photoluminescence (PL) and a lower noise floor.^[29]

All-optical temperature measurement methods, based on the temperature-dependent shift of the luminescence spectra of color centers in diamond, such as silicon-vacancy (SiV), germanium vacancy (GeV), and tin vacancy (SnV) with strong zero-phonon line (ZPL), can be used.^[30] These methods are promising, but for the moment, apart from one very invasive experiment,^[31] there are few reported biosensing applications. For instance, in a notable experiment,^[32] gold nanorod-fluorescent ND hybrids were used as nanoheater/nanothermometer for studying living human embryonic kidney cells. In this case the NDs registered the temperature variation associated with the heating obtained by local laser irradiation of the nanorods. In another recent experiment,^[33] SiV in NDs were used to for imaging and temperature measurement in HeLa cells, even if only the average temperature of the bath (by controlling the incubator temperature) was measured, without single-cell resolution. It must be stressed anyway that, in both the above mentioned works, the temperature variation was induced by the experimenters (i.e., via laser irradiation or by changing the incubator temperature) and no authentic biological phenomenon was measured. Notwithstanding the undoubted promising perspective of all-optical methods, currently the most promising approach exploits nitrogen-vacancy (NV) centers.^[29]

For these reasons, NV color centers in ND combined with optically detected magnetic resonance (ODMR) technique can assume a dominating position in thermometry^[34] for biological application.^[7,35,36] Nevertheless, ODMR measurements protocols

are based on microwave irradiation of the samples, which makes this technique more elaborated and requires awareness on the exploitable optical and microwave power providing the required sensitivity without damaging the cells.

ND was used for the first time in *in vitro*^[37] measurements (of a heated gold nanoparticle inside a cell). Subsequently, an *in vivo* experiment was performed inside *Caenorhabditis elegans* worms, reaching a sensitivity as low as $1.4\text{ }^{\circ}\text{C Hz}^{-1/2}$. In the same experiment, thermogenic responses have been monitored during the chemical stimuli of mitochondrial uncouplers.^[16] Temperature gradients have been mapped at the subcellular level into a single human embryonic fibroblast^[7]; intracellular temperature mapping has been performed also in cultured primary cortical neurons, employing micro electrode arrays (MEAs) to demonstrate that the presence of NDs in primary cortical neurons does not elicit a neurotoxic response,^[38] in good agreement with our previous findings.^[26] Finally, heterogeneous temperature variations have been coupled with Ca^{2+} increases in HeLa cells.^[39]

Here, for the first time, we quantify the direct correlation of intracellular temperature variations with the modulation of neuronal activity. We demonstrate that sensors based on NV centers in NDs, interrogated via ODMR techniques, reveal up to $1\text{ }^{\circ}\text{C}$ temperature variation when the spontaneous firing of hippocampal neurons is potentiated by picrotoxin or the $0.5\text{ }^{\circ}\text{C}$ temperature decrease when the neuronal activity is silenced by a solution containing tetrodotoxin and cadmium chloride.

2. Results

In the presented experiments, temperature variations, associated to different patterns of neuronal activity, were detected using an ODMR measurement protocol, consisting of simultaneously applying a variable frequency microwave field and nonresonant laser radiation to the sample while acquiring the PL intensity (photon counts) emitted by a single ND.

The ODMR protocol used is based on the possibility to optically detect the negatively charged NV^{-} center's spin state and optically pump it into the $|m_s = 0\rangle$ sublevel. The mechanism is described as follows.

2.1. Optically Detected Magnetic Resonance (ODMR)

Depending on the NV electron spin state, two different decaying paths are possible. If the system is in the state $|m_s = 0\rangle$, then a spin preserving transition occurs with single-photon emission at wavelength $\lambda = 637\text{ nm}$ (ZPL). This transition is cyclic and one detects high PL intensity when continuously illuminating the NV center.

If the electron spin state is instead $|m_s = \pm 1\rangle$, two possible decay paths are possible. The first one is again spin-preserving and leads to the previously-described PL emission. The second one is nonspin-preserving and the system ends up in the spin state $|m_s = 0\rangle$ of the ground level (see **Figure 1a**). In this latter case, the system relaxes through the two metastable singlet spin states, namely, ^1A and ^1E . These have a transition wavelength in the infrared range, $\lambda = 1046\text{ nm}$. This process is referred as “intersystem-crossing” because it involves a transition between

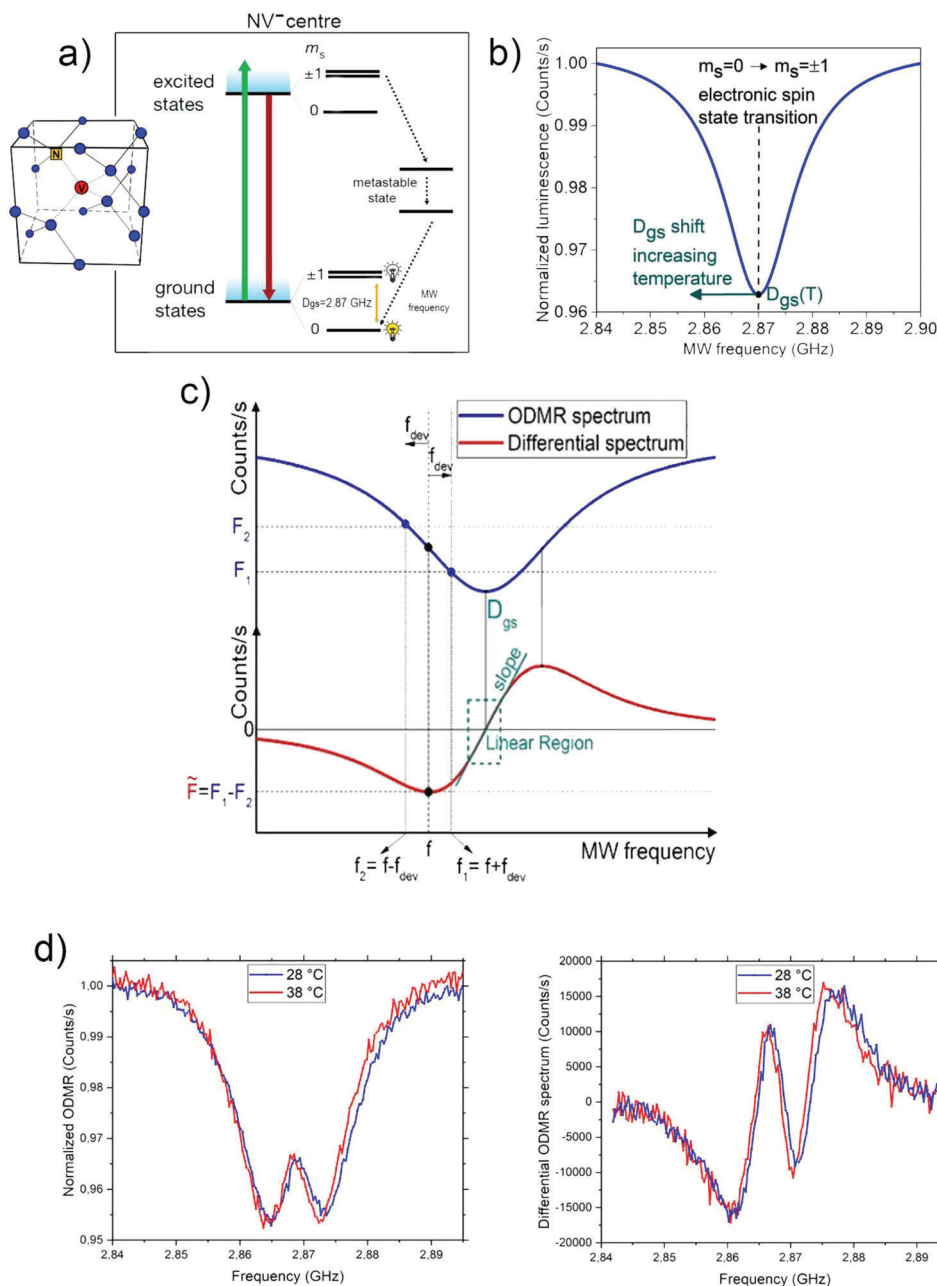


Figure 1. a) NV^- state transition that occurs after laser excitation and MW excitation. The coupling of the states $|m_s = \pm 1\rangle$ with the metastable level generates a statistically lower PL emission than the $|m_s = 0\rangle$ one. b) PL collected from the NV^- center as a function of the MW frequency. A dip in correspondence of the zero-field splitting D_{gs} (resonance frequency of the undisturbed NV^- center, at room temperature) can be observed. c) Sketch of the differential measurement. From the ODMR spectrum (upper part of the figure) the differential spectrum (lower part of the figure) is derived taking, for every value of the microwave (MW) frequency, the difference $\tilde{F} = F_1 - F_2$ in PL between two points (F_1, F_2) separated by $2f_{\text{dev}}$. \tilde{F} is zero at the two extremes of the spectrum and at the resonant frequency D_{gs} . Around D_{gs} there is a region where $\Delta\tilde{F}$ depends linearly on ΔD_{gs} through the differential spectrum slope. d) Example of ODMR and differential ODMR spectra at two different temperatures.

the two electronic states with different states spin multiplicity. Due to the presence of this nonradiative decay path the spin state $|m_s = \pm 1\rangle$ is less luminescent with respect to $|m_s = 0\rangle$ one. Remarkably, the above-explained feature allows the optical read-out of the spin state of the NV center at room temperature. This is achieved by the method of ODMR which consists in applying a microwave field of variable frequency, simultaneously with irra-

diation of a nonresonant laser able to excite the electronic state. In this case, a 532 nm pump laser is required. When the microwave frequency matches the exact resonant frequency D_{gs} between the $|m_s = 0\rangle$ and $|m_s = \pm 1\rangle$ states, less PL is collected and therefore a fluorescence dip is observed in the ODMR spectrum (see Figure 1b). This allows the optical readout of the spin state.

It is important to underline that when NDs are used as sensors instead of bulk diamonds, the degeneration of the $|m_s = +1\rangle$ and $|m_s = -1\rangle$ levels are removed by mechanical stress. In this case, two dips are observed in the ODMR spectrum. Both of them show a shift in the same direction in the resonance frequency as the temperature varies (Figure 1d).

By applying this protocol, a dip in the collected PL intensity is observed when the microwave frequency matches the exact resonant frequency D_{gs} between the $|m_s = 0\rangle$ and $|m_s = \pm 1\rangle$ electronic spin states of the NV center. Since the value of D_{gs} depends on temperature, this technique allows determining the temperature at the ND location by measuring a frequency shift.

The temperature variation ΔT measured with the ND sensor is estimated through a direct PL change observation according to the equation

$$\Delta T = \frac{\Delta \tilde{F}}{\text{slope} \cdot \partial D_{gs} / \partial T} \quad (1)$$

where $\Delta \tilde{F}$ is the actual measured physical signal (difference in the photocounting rate), slope represents the constant of proportionality that connects $\Delta \tilde{F}$ to the resonance frequency shift ΔD_{gs} . Finally, $\partial D_{gs} / \partial T$ represents the coupling constant. Under ambient conditions the coupling constant $\partial D_{gs} / \partial T$ is estimated as $-75 \text{ kHz } ^\circ\text{C}^{-1}$ for a bulk diamond (see the Experimental Section). The sensitivity of the measurement method is about $3 \frac{^\circ\text{C}}{\sqrt{\text{Hz}}}$, comparable to the state of the art in detection of biological signals with NV sensors in NDs.

2.2. Differential ODMR Spectrum Experimental Measurement Technique

In the differential spectrum measurement technique applied in this experiment, the full ODMR spectrum was acquired only once for 60 s. The data was postprocessed creating the differential spectrum (see Figure 1c). In correspondence to each microwave scanning frequency f , a differential photoluminescence (PL) value \tilde{F} was associated as follows: $\tilde{F} = F(f_1) - F(f_2)$.

Here F represents the PL collected from the ND sensor, $f_1 = f + f_{\text{dev}}$, $f_2 = f - f_{\text{dev}}$, and f_{dev} is a frequency deviation chosen in order to optimize the differential graph, in our case $f_{\text{dev}} = 2 \text{ MHz}$.

The method advantage is that in correspondence of temperature variations, for a fixed frequency f the differential signal \tilde{F} results linearized with respect to frequency shift around the resonant frequency D_{gs}

$$\Delta \tilde{F} = \text{slope} \cdot \Delta D_{gs} \quad (2)$$

The slope value was then obtained through a linear regression from the differential spectrum.

The differential signal \tilde{F} was acquired only at one frequency chosen in the linear region of the differential spectrum. The signal \tilde{F} was acquired in two steps: in the first step the frequency generator was set at f_1 for 50 ms; in the second step the frequency was switched to f_2 for the same sampling time. Between the two step a waiting time of 10 ms was set. The cycle was repeated for 500 times (effective repetition rate 8.3 Hz). Any variation $\Delta \tilde{F}$ recorded was attributable to a shift in the resonance

frequency ΔD_{gs} and therefore to a temperature variation ΔT , according to Equation (1).

This differential method is analog to probe the fluorescence at the inflection point of the ODMR spectrum, see Figure 1a. It removes the effects of extrinsic background signal and mitigates the effects of variations in the NV⁻ fluorescence and in resonance linewidth.^[40] To further reduce the effect PL stability and the spatial inhomogeneities of the microwave field we use a very stable laser and specially designed planar broadband antenna, which provided a strong, homogeneous, electromagnetic radiation.^[41]

Compared to four frequency method used,^[7] our method is of simpler experimental implementation and it is suitable when no signal from magnetic field is expected. The fluctuating magnetic field in our case represents a source of uncertainty.

2.3. Temperature Variation Measurement

The thermometric apparatus used for the experiment was based on a single-photon-sensitive confocal microscope compatible with ODMR measurement. A simplified scheme of the apparatus is shown in Figure 2a. The optical excitation power provided by a CW 532 nm laser (Coherent Prometheus 100NE, Relative Intensity Noise $< -90 \text{ dB Hz}$, 2nd harmonics) was $< 1 \text{ mW}$ and the acquisition time of all PL measurements was 60s. These values were chosen as a trade-off between the fast measurement and the precise temperature estimation. We underline that our choice guarantees cell viability and, in principle, allows for time-resolved measurements on the scale of metabolic processes.

To exploit the ODMR protocol for measuring intracellular temperature variations, hippocampal neurons (10 days in vitro) were incubated for 5 h with $0.6 \mu\text{g mL}^{-1}$ NDs (average diameter 185 nm, PDI 0.115), which is far below the cytotoxicity threshold ($< 250 \mu\text{g mL}^{-1}$), as demonstrated in a previous work of our group,^[26] and by,^[42] which tested the ND cytotoxicity up to $250 \mu\text{g mL}^{-1}$. ND internalization (Figure 2c) was assessed by means of standard confocal imaging (see the Experimental Section).

In the following, all measurements were performed after checking that the PL counts were stable and no unwanted movement (drift, displacement, Brownian motion) of the NDs took place.

To detect the temperature variations associated with different patterns of neuronal activity, recordings were performed in three conditions (Figure 2b): i) in the presence of external Tyrode solution (CTRL), since in this condition the hippocampal network was spontaneously firing,^[28] ii) after addition of $100 \mu\text{M}$ of picrotoxin, a selective GABA_A inhibitor, which is known to drastically potentiate the neuronal firing activity,^[43] iii) after subsequent addition of $0.3 \mu\text{M}$ tetrodotoxin (TTX) and $500 \mu\text{M}$ cadmium chloride (Cd), to inhibit the spontaneous firing. Bath temperature was kept at $37 ^\circ\text{C}$ and the photocounting rate was performed from internalized NDs. With reference to the above conditions, a more detailed account of the three measurements condition follows hereby.

- Condition (i): To exclude that the perfusion system could induce some temperature variations, the photocounting rate \tilde{F} from an internalized ND was measured before and after perfusing the cells with Tyrode solution (CTRL, in Figure 2d). From

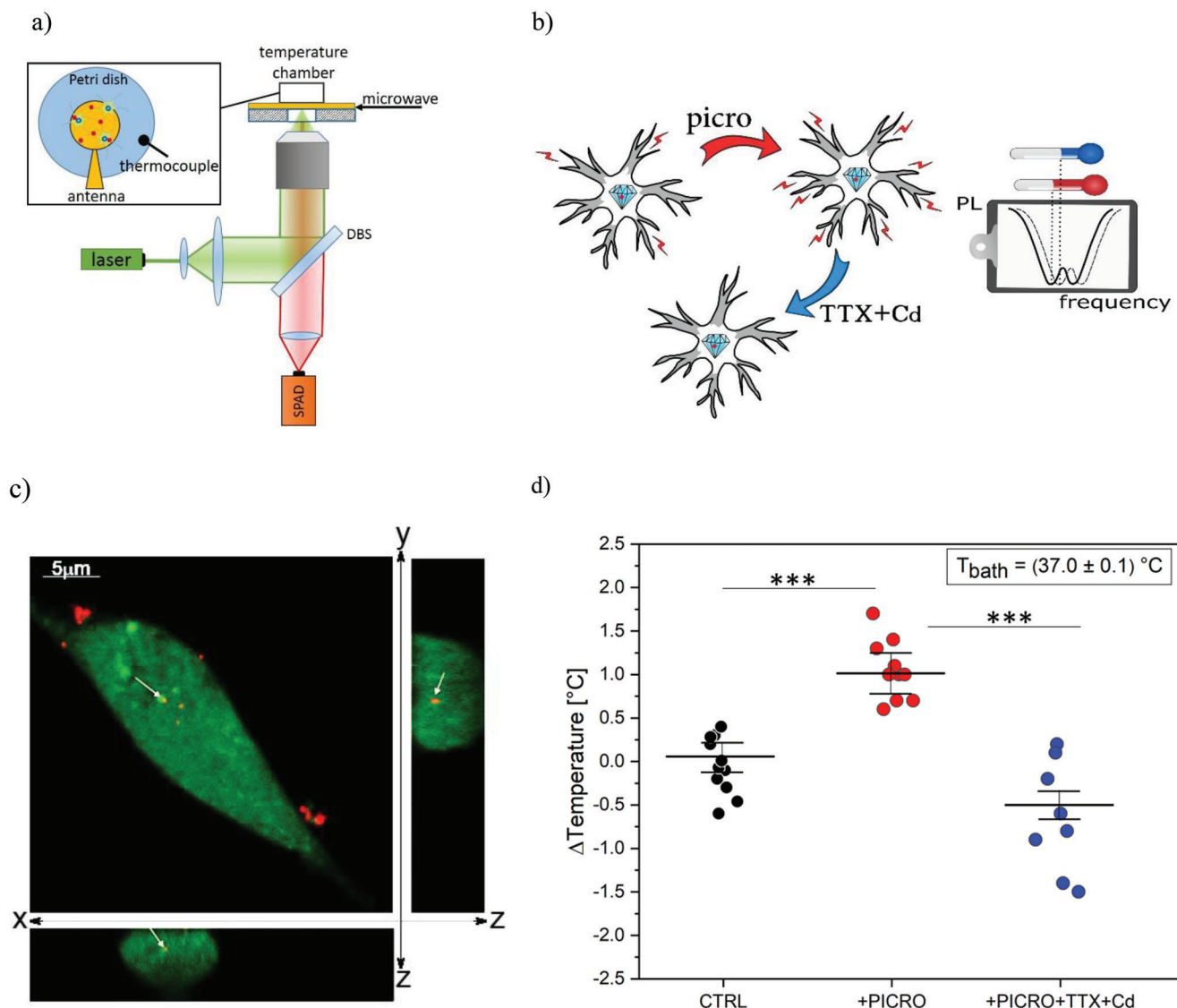


Figure 2. Illustration of the experiment. a) Simplified scheme of single-photon confocal ODMR setup. b) The ODMR measurements are performed under control conditions (CTRL), after stimulation with picrotoxin and after the addition of TTX+Cd. The frequency shift in the ODMR spectrum (dashed line) is associated with the temperature variation recorded by the ND sensor. c) Confocal fluorescence micrograph of hippocampal neurons incubated with $0.6 \mu\text{g mL}^{-1}$ ND for 5 h. The cytoplasm is stained in green, the red emission is from NDs. The entire field and cross-sections (XZ and YZ) are shown. White arrows show one internalized ND. d) Boxplot of temperature variations with standard deviations in the presence of saline Tyrode solution (CTRL, black circles), after addition of picrotoxin (PICRO, red circles), after addition of tetrodotoxin and cadmium chloride (TTX+Cd, blue circles), see text for details. Statistical difference is indicated by the asterisks (***, $p < 0.0001$)

the photoluminescence difference $\Delta\tilde{F}$, the temperature variation was estimated according to Equation (1). In these conditions we revealed an average temperature variation $\Delta T = (0.05 \pm 0.15)^\circ\text{C}$ (weighted average evaluated on a sample with a numerosity $N = 11$), proving that no significant temperature variations are associated with thermal exchanges of the perfusion system.

After this preliminary test, the next step was to assess whether changes in neuronal firing could be associated to temperature variations.

- Condition (ii): ΔT was estimated by comparing \tilde{F} before and after perfusing the cells with a picrotoxin-enriched Tyrode solution. The addition of the GABA_A inhibitor caused a significant temperature increase, $\Delta T = (1.02 \pm 0.24)^\circ\text{C}$ ($N = 10$), associated with the increased firing rate (Figure 2a). As a more quantitative corroboration of our conclusions, a thorough statistical uncertainty analysis was performed (see the Experimental Section) to confirm that a significant localized temperature variation occurs in a neuron deriving from sustained firing activity (1.12×10^{-8} significance in a Welch *t*-student test).

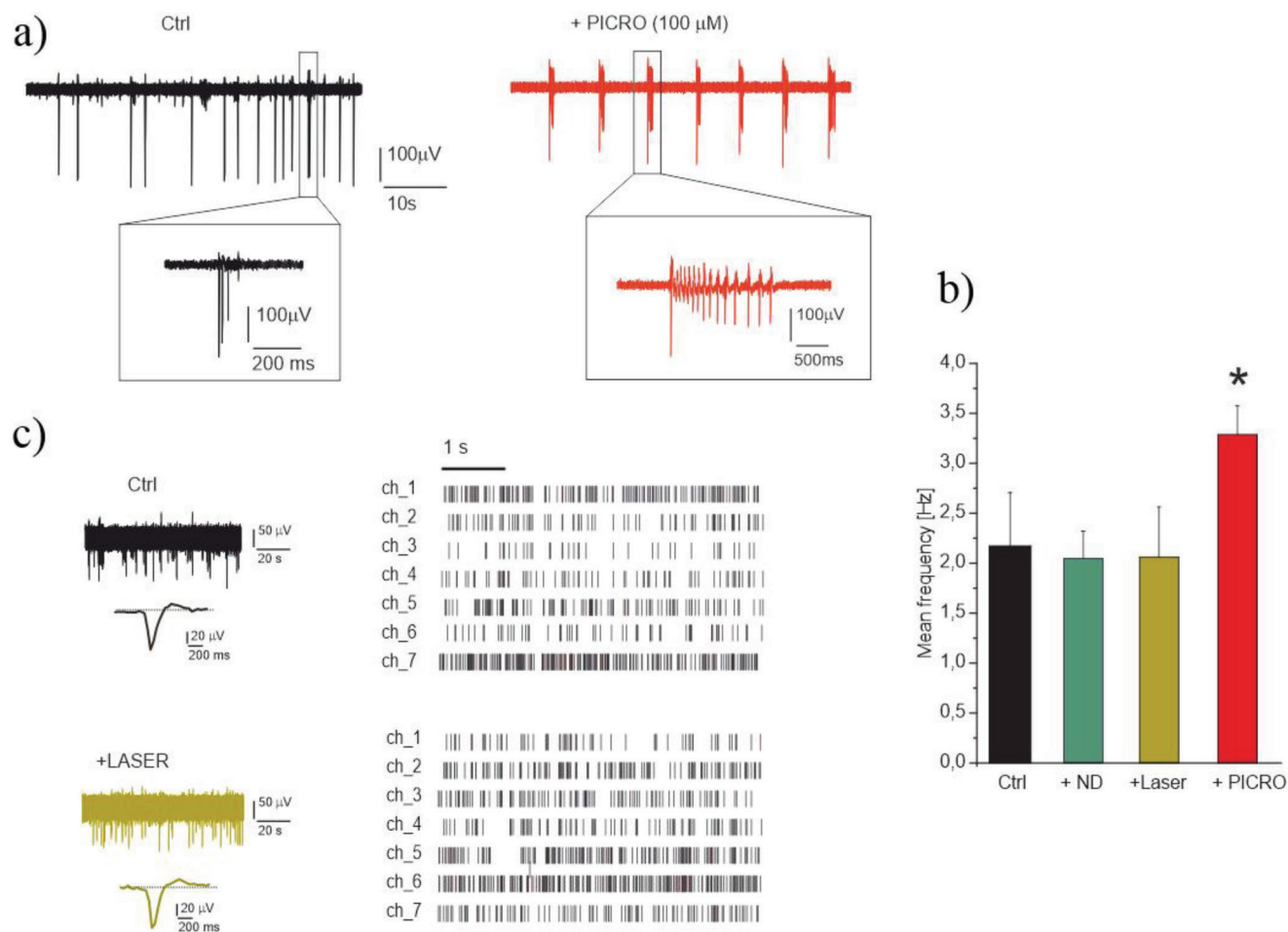


Figure 3. Laser exposure does not affect the hippocampal neurons. a) modulation of the firing activity by PICRO (MEA recordings): representative traces from the same electrode under control condition, + PICRO. Insets: higher magnification of single spikes and bursts. b) Histogram of mean frequency in the different experimental conditions. The statistical difference of PICRO respect to other conditions is indicated ($p < 0.05$, *). c) Left: Representative traces in control condition and after laser irradiation and (right) corresponding raster plot. In the raster plot, 7 representative channels (ch_1÷ch_7) are shown.

- Condition (iii): network activity was silenced by means of the Tyrode solution enriched with TTX+Cd. In this case, ΔT was measured by comparing \tilde{F} before and after perfusing the cells with picrotoxin + TTX+Cd solution. Under this last condition, a significant temperature decrease $\Delta T = (-0.50 \pm 0.17)^\circ\text{C}$ ($N = 8$) was revealed (Figure 2d) with a 2.21×10^{-6} significance in a *Welch t*-student test (see the Experimental Section). These data demonstrate that both potentiation and silencing of the neuronal network activity could be assessed by temperature variations and that the hippocampal network, exhibiting basal spontaneous activity, displays higher temperatures than the completely silenced network.

Another set of experiments was carried out for measuring the average temperature variation associated to noninternalized ND before and after perfusing the cells with picrotoxin solution: in this case no significant difference with respect to the control conditions was found: $\Delta T = (-0.04 \pm 0.23)^\circ\text{C}$ ($N = 7$). This crossover trial excluded that temperature variation can be due to other external factors than the drug-potentiated neuronal activity.

Furthermore, it has been tested whether the laser exposure, microwave radiation and incubation with NDs could affect the spontaneous firing activity of hippocampal neurons during ODMR measurement protocol (as detailed in the Experimental Section). As shown in Figure 3, both the spontaneous firing rate and the action potential waveform were not significantly altered by laser and ND exposure, confirming that cell excitability and ion channel functioning are preserved, in good agreement with our previous findings.^[26]

Finally, in parallel with the thermometry experiment, the effect of GABA_A receptor blockade on burst-firing of hippocampal neurons was assessed by comparing the spontaneous burst ratio of cells responses before and after application of picrotoxin. These recordings have been performed by means of conventional MEAs (MCS, multichannel system). An expected significant increase of the spontaneous activity,^[44] (from 2.1 ± 0.3 to 3.4 ± 0.3 Hz), which is associated to disinhibition of GABA_A receptors (Figure 3a), and a complete silencing of the network in the presence of the Na⁺ and Ca²⁺ voltage-dependent channel blockers TTX and Cd was observed. The data presented allowed to conclude that the

increase in temperature recorded in the experiment is directly related to the altered firing activity of hippocampal neurons.

3. Conclusion

Intracellular localized temperature gradients are associated with metabolic activity and with a variety of reactions and intracellular processes.^[45,46] Real-time mapping of intracellular subtle temperature gradients and event-driven increased temperature represents a tool of the utmost interest for monitoring the functional activity of the cells, for identifying localized signaling under physiological conditions and for exploitation as a diagnostic tool.

Here we applied the ODMR technique to cultured hippocampal neurons for monitoring temperature variations in different conditions of network excitability. We provided evidence that a significant temperature increase can be correlated with the altered firing activity of cultured hippocampal neurons, in our case induced by picrotoxin, and that this phenomenon can be successfully observed at the single-cell level exploiting nanosensor based on NDs.

It is worth noticing that picrotoxin-induced disinhibition primarily alters cell excitability, but the increased action potential firing activity may in turn alter intracellular pathways: since we cannot predict whether NDs are localized at the plasma membrane or at the intracellular level, the detected temperature increases are indeed induced by picrotoxin but can be associated to membrane-delimited or intracellular processes. Interestingly, a reduction of the network activity is detectable as a $\Delta T = (-0.50 \pm 0.17)^\circ\text{C}$ temperature decrease. Another relevant finding is that our method is suitable to distinguish the basal spontaneous firing rate,^[26,47–49] from the condition in which the network activity is completely silenced.

Thus, this approach may uncover different degrees of neuronal excitability.

We underline that the possibility of slightly improving the setup and the measurement technique (which being a first version is not yet completely optimal) can lead to a further enhancement of the sensor sensitivity. In perspective, it is reasonable to foresee more than a one-order of magnitude improvement in sensitivity with respect to the current condition by accounting for three main improvements of the system: 1) implementing orientation tracking of NDs in order to apply transversal bias field scheme as already demonstrated in bulk diamond,^[50] which allows a factor 3 of scaling in the temperature sensitivity in EM-insensitive condition; 2) particle tracking would also allow for longer measurement time, for instance an increase of the measurement time of a factor 10 would result in another factor 3 scaling in sensitivity; 3) obtaining samples of NDs with an increased number of NV centers would result (below saturation threshold) in a further improvement of sensitivity (also in this case, an increase of a factor 10 in the interrogated centers would result in a factor 3 improvement in the sensitivity).

Finally, together with the above mentioned upgrades, improving the ND fabrication, resulting in increased coherence, would allow further improvement of the sensitivity, realistically rendering the system in perspective sensitive to $< 0.1^\circ\text{C}$ variations. We underline that these nanosensors, carefully prepared and selected, are able to provide a fast temperature measurement with

extraordinary spatial resolution, in perspective even below the diffraction limit.^[51]

The action potential generation and propagation is not the unique energy-requiring process involved in neuronal activity, as this may also involve maintenance of the membrane resting potential, neurotransmitter release and uptake, vesicular recycling and presynaptic Ca^{2+} currents.^[46] The firing activity is correlated with the total energy consumed by neuronal activity. This has been calculated from anatomic and physiological data,^[45] and experimentally verified using fMRI techniques.^[52] Thus, our results prompts further studies to assess whether the observed temperature increase during perfusion with picrotoxin is ascribed to sustained firing activity and/or potentiated cell metabolism.^[44]

By means of confocal microscopy observation, we demonstrate that 5 h exposure to ND is enough to promote ND internalization and that action potential waveform remains unaffected after laser and microwave irradiation, confirming that the applied protocol for sensing temperature preserves cell excitability and ion channel functioning^[26] (with perspectives for “in vivo” studies).

The measured temperature increases can be used to reveal the onset of different intracellular processes other than membrane-delimited pathways, likely involving an altered cell metabolism as here was demonstrated with picrotoxin. Thus, our future goals will be devoted to functionalizing NDs to subcellular compartments, to detect thermogenesis at specific subcellular sites.

These results, backed by a thorough analysis of other possible alternative causes of temperature variation, pave the way to a systematic study of cell activity with impacts ranging from a better insight on current unknowns associated with cells functioning, such as, e.g., the aforementioned discrepancy between experimental data and thermal diffusion models, to the research on specific pathologies.

Our findings also prompt further applications where ongoing advances in microelectrode array technology (MEA), combined with quantum sensing paves the way for experiments that take advantage from the synergy of the two techniques, such as synchronized measurements of cellular activity with metabolism processes or propagation of electromagnetic signals.

4. Experimental Section

Experimental Setup: The thermometric apparatus used for this experiment (**Figure 4**) was based on an Olympus IX73 inverted microscope, in which optical elements to implement single-photon confocal imaging and microwave control for ODMR measurements were integrated. A CW 532 nm laser (Coherent Prometheus 100NE, noise reduced regime, 2nd harmonics), attenuated down to 1 mW, was used to excite the NV centers in the NDs. Then an acousto-optic modulator (AOM), controlled by a pulse generator (Pulse streamer, Swabian Instruments), was applied to the laser emission to have the cell irradiated only during the measurement. Finally, a 60× air microscope objective (Olympus UPLANFL, NA = 0.67) was used for both excitation and photoluminescence (PL) collection. The spot size of the focused laser beam was $\approx (1.2 \times 1.3) \mu\text{m}^2$. The NV PL was filtered by a 567 nm dichroic mirror, a 650 nm long-pass filter and a Notch filter centered at 532 nm to remove the residual green laser scattering, and then collected by a single photon avalanche diode (SPAD, SPCM-AQR 15, Perkin Elmer). The emission rate from a single ND was around 300 k Counts s^{-1} .

The Petri dish, containing the cell culture with NDs, was placed in a closed incubation chamber with a temperature control (Okolab Temperature Controller, temperature stability 0.1°C). The sample could be moved via a manually or software-controlled piezoelectric XYZ scanning stage

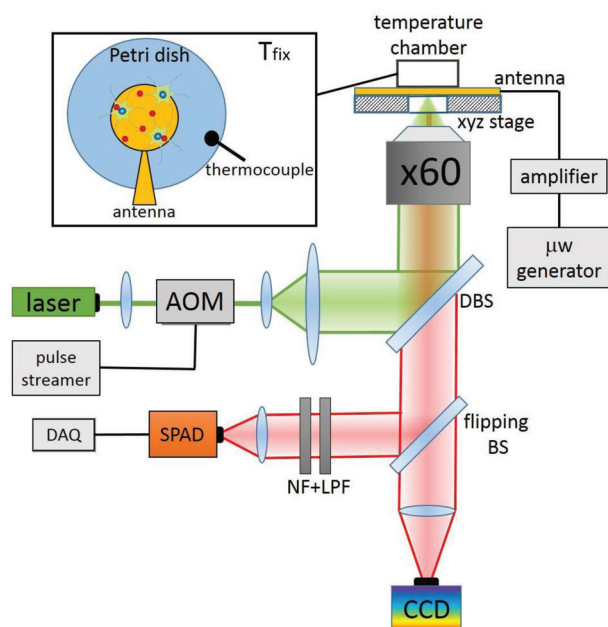


Figure 4. Experimental setup scheme. AOM: acousto-optic modulator, DBS: dichroic beam splitter, LPF: long-pass filter, NF: notch filter, DAQ: data acquisition board, SPAD: single-photon avalanche diode. The cells are cultured on a Petri dish, placed inside an incubator (temperature chamber), which can be moved by means of a three-axis piezoelectric system (xyz stage). The temperature inside the closed incubation chamber is controlled by a PID and measured by a thermocouple.

allowing selecting the area of interest. The output signal from the SPAD was fed to a data acquisition board system (National Instruments, USB-6343 BNC).

To implement the ODMR measurements, a microwave source (Keysight N5172B) was used. The output signal was then amplified (Mini-Circuits, ZHL 16W 43+) to a power of 20 dBm and fed to a homemade planar broadband antenna, which provided a strong, homogeneous, electromagnetic radiation. The Petri dish was placed on the top of the antenna.

Experimental Procedure: The experimental procedure for detecting temperature variation using NV centers in NDs was the following.

A Petri dish containing cultured hippocampal neurons (10 DIV), previously exposed to NDs, was positioned inside the single-photon confocal microscope incubation chamber. Using the motorized stage, the sample was scanned by incident laser ($P < 1$ mW, $\text{RIN} < -90$ dB Hz^{-1}) in order to select a single ND inside a cell. The ODMR spectrum was acquired for 60 s and the data were postprocessed to create the differential. Then, the microwave frequency was set in accordance with the minimum of the ODMR spectrum (zero of the differential spectrum). The differential signal of luminescence at this frequency was acquired for 60 s. The microwave field before and after data acquisition was always turned on to avoid possible heating transient processes.

In a successive step, solutions containing 100 μM microtoxin and then 300 nM TTX + 200 μM CdCl_2 were added to the medium. The measurement of the differential signal was repeated at the same resonant frequency as in the previous step. Finally, the ODMR spectrum was reacquired for 400 s, recreating a new differential spectrum in order to improve the statistics and to evaluate the linear region slope with lower uncertainty. The temperature variation ΔT was evaluated through a direct PL change measurement according to equation

$$\Delta \tilde{F} = \text{slope} \cdot \partial D_{\text{gs}} / \partial T \cdot \Delta T \quad (3)$$

Table 1. Summary of NDs ($N = 6$) coupling constant evaluations and their associated uncertainty, obtained through the uncertainty propagation.

$\frac{\partial D_{\text{gs}}}{\partial T} \left[\frac{\text{kHz}}{^\circ\text{C}} \right]$
79 ± 6
63 ± 9
76 ± 12
86 ± 12
72 ± 8
81 ± 10

Here $\Delta \tilde{F}$ represents the differential signal variation (difference in the photon counting rates), evaluated at the linear region of the differential spectrum and associated with a temperature variation ΔT . The slope represents the constant of proportionality that connects $\Delta \tilde{F}$ to the resonance frequency shift ΔD_{gs} . Finally, $\partial D_{\text{gs}} / \partial T$ represents the coupling constant.

Experimental Procedure—Estimation of $\partial D_{\text{gs}} / \partial T$: Under ambient conditions the coupling constant $\partial D_{\text{gs}} / \partial T$ is estimated as 75 $\text{kHz } ^\circ\text{C}^{-1}$ for a bulk diamond.^[53,54] For NDs this constant varies due to the different strain splitting and, in principle, should be calibrated.

The method to obtain $\partial D_{\text{gs}} / \partial T$ was the same adopted for the cell temperature measurement, with the difference that in this case ΔT was not induced by a substance perfusion but forced by the incubator chamber's heater, and that ΔT is measured by a thermocouple. The procedure was the following. The NDs were placed on the Petri dish with distilled water. The ODMR spectrum was acquired and so was the differential spectrum by postprocessing the data, see above. The linear region slope of the differential spectrum was obtained by performing a linear regression. The microwave generator was set at the resonant frequency D_{gs, T_0} that occurred in the initial temperature condition reached in the incubator chamber, at which the differential spectrum signal \tilde{F} was zero. The incubator temperature was varied, recording it with the thermocouple. The new value of the differential signal was read. Finally, $\Delta \tilde{F}$ was plotted as a function of the temperature increase ΔT recorded by the thermocouple. Through a linear regression the constant of proportionality b was evaluated, i.e., the quantities mentioned obey the following physical relationship

$$\Delta \tilde{F} = b \cdot \Delta T \quad (4)$$

where

$$b = \text{slope} \cdot \partial D_{\text{gs}} / \partial T \quad (5)$$

By inverting the last equation, the quantity $\partial D_{\text{gs}} / \partial T$ was estimated. The results are shown in Table 1. Both the arithmetic mean and the weighted mean coincide: $\partial D_{\text{gs}} / \partial T = (-76 \pm 4) \text{ kHz } ^\circ\text{C}^{-1}$. We used this estimated value for $\partial D_{\text{gs}} / \partial T$ and the associated uncertainty in the data analysis.

Cell Preparation and Nanodiamonds (ND) Labeling: Hippocampal neurons were obtained from C57BL/6 16-day embryos. All animals were housed under a 12 h light/dark cycle in an environmentally controlled room with food and water ad libitum. All experiments were conducted in accordance with the European Community's Council Directive 2010/63/UE and approved by the Italian Ministry of Health and the Local Organism responsible for animal welfare at the University of Turin (Authorization 695/2020-PR). Hippocampus was rapidly dissected under sterile conditions, kept in cold HBSS (4 $^\circ\text{C}$) with high glucose, and then digested with papain (0.5 mg mL^{-1}) dissolved in HBSS plus DNase (0.1 mg mL^{-1}). Isolated cells were plated at density of 1200 cells mm^{-2} onto the MEA and 1000 cells mm^{-2} onto the glass Petri dishes. Both the MEAs and the dishes were previously coated with poly-DL-lysine and laminin, this allowed the neurons to adhere to the center of the device by using a ring made of Sylgard 184 (Dow Corning), which was removed after 4 h. The cell medium is composed of 1% penicillin/streptomycin, 1% glutamax, 2.5% fetal bovine serum, 2% B-27 supplemented neurobasal medium. The neurons were

incubated in a humidified 5% CO₂ atmosphere at 37 °C. Recordings were carried out at 10–12 days in Vitro (DIV).

The initial ND solution (1 mg mL⁻¹, MiliQ water) was sonicated for 5–10 min (100 W power, 80 kHz frequency), in order to separate diamond particle clusters into single NDs. After sonication, the 60 µL of solution was diluted with 1 mL of Tyroide to obtain a final ND concentration of 0.6 µg mL⁻¹ which was poured into the Petri dish. The dish was exposed to NDs for 5 h in order to allow NDs internalization. Once the dish was extracted from the incubator, the cell medium was removed and replaced with 2 mL of Tyrode solution.

Micro Electrode Array Recordings: Multisite extracellular recordings were performed using the MEA-system, purchased from Multi-Channel Systems (Reutlingen, Germany). The 60 electrodes array (TiN) was composed of an 8 × 8 square grid with 200 µm inter-electrode spacing and 30 µm electrode diameter. Data acquisition was controlled through MC_Rack software (Multi-Channel Systems Reutlingen, Germany), sampling at 10 kHz. Experiments were performed in a non-humidified incubator at 37 °C and with 5% CO₂, maintaining the culture medium. Before starting the experiments, cells were allowed to stabilize in the non-humidified incubator for 5 min; recording of the spontaneous activity was then carried out for 120 s. Mean frequency has been evaluated over 120 s recording. The data are analyzed using Neuroexplorer software (Nex Technologies, Littleton, MA) after spike sorting operations.

Confocal Image Acquisition: After 5 h exposure to ND (0.6 µg mL⁻¹ NDs), the cytoplasmic labelling dye (CellTracker Green CMFDA, ThermoFisher,) was added to the medium. This allowed to identify the cell boundaries of cultured hippocampal neurons (10 DIV) together with the internalized NDs, characterized by a red fluorescent emission. For standard confocal imaging, hippocampal neurons were plated on 35 mm dishes (ibidi GmbH, Planegg/Martinsried, Germany). Cells were analyzed using a confocal laser scanning microscope Leica TCS SP5, equipped with an argon ion and a 561 nm DPSS laser. Cells were imaged using a HCX PL APO 63x/1.4 NA oil immersion objective at a pixel resolution of 0.08 × 0.08 × 0.3 µm. The luminescent emission from the fluorescent NDs was excited by 561 nm laser, while the emission was collected in the 650–750 nm spectral range. The same excitation wavelength was ineffective in untreated neurons. Green fluorescence for intracellular staining was obtained by 488 nm wavelength. Image analysis was performed using ImageJ software.

Monodisperse ND Preparation: NDs were supplied by Microdiamant Switzerland (MSY 0-0.25, containing ≈100–200 ppm of natural nitrogen impurities) and treated as described previously.^[55] Briefly, the NDs were oxidized by air oxygen at 510 °C for 5 h and then wet oxidized in a HF:HNO₃ 2:1 v/v stirred mixture at 160 °C for 2 days in a PTFE container. The acids were removed using consecutive centrifugation/washing and the resulting pure oxidized NDs were lyophilized. The monodisperse NDs (hydrodynamic diameter 205 nm) were isolated using differential centrifugation in water based on gradual centrifugation/dilution steps, combination of the separated pellets, followed by their lyophilization.

Fluorescent NDs Irradiation and Oxidation: A total of 330 mg of the monodisperse ND was irradiated at 870 °C,^[56] in an external target for 80 h with a 15.7 MeV electron beam (2.5 × 10¹⁹ particles cm⁻²) extracted from the MT-25 microtron.^[57] After irradiation, the NDs (315 mg) were annealed at 900 °C for 1 h under argon atmosphere and subsequently oxidized in air for 5 h at 510 °C. The resulting fluorescent NDs were wet oxidized using a 2:1 v/v mixture of HF:HNO₃, washed and lyophilized, providing 212 mg of NDs with NV centers (yield 64%). Before use, the lyophilized NDs were redispersed in MiliQ water using cup horn sonication to concentration 1.0 mg mL⁻¹.

Dynamic Light Scattering: The hydrodynamic particle diameter was measured using a Zetasizer Nano ZS (Malvern Instruments) in disposable transparent cuvettes. The samples were measured at Room Temperature with a concentration of 0.05 mg mL⁻¹ and a total volume of 1 mL.

Nanodiamond Sensor Sensitivity: In order to evaluate the sensitivity of our ND-based sensors, a control calibration test was performed. The NDs were deposited on a glass slide and inserted into the temperature chamber of the single-photon confocal microscope. The differential signal was evaluated (10 measurements with duration 60 s) at three different temper-

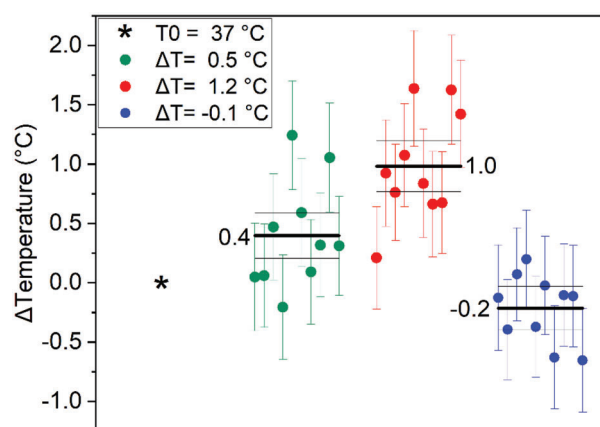


Figure 5. Validation of temperature detection by ND sensor. The legend box shows the temperature values recorded by the thermocouple. The box plot shows the temperature values recorded by the ND sensor. The mean and its uncertainty (standard deviation divided by the square root of repeated measurements) are reported as horizontal lines in each data set ($N = 10$, 60 s acquisition). The starting point is highlighted as an asterisk. The incubator temperature at the end of the cycle is consistent with the initial temperature within the incubator stability (0.1 °C).

atures and then compared with the readout of a standard thermocouple. **Figure 5** shows the response of the ND sensor to a thermal cycle with steps 0.5 °C, 1.2 °C (chamber temperature stability 0.1 °C). The average values are shown in the figure next to each dataset. The results are in agreement with the bath temperature recorded by the thermocouple, shown in the legend box. This control test highlights the sensitivity of the measurement method, capable of discriminating a variation of 0.5 °C. Our sensitivity is about $3 \frac{^{\circ}\text{C}}{\sqrt{\text{Hz}}}$ and is estimated according to the following equation

$$\eta = \frac{\sigma_{\bar{F}} \sqrt{\Delta t}}{\text{slope } \gamma_T} \quad (6)$$

where $\sigma_{\bar{F}}$ represents the standard error of the mean of the variation of the differential counts and Δt represents the measurement time.

Statistical Analysis: As detailed in the main text, the experiment was repeated collecting a sample of $N = 11$ repeated measurements, revealing any temperature rise from a ND inside the cell before and after Tyrode's solution perfusion. In the main test this is referred to as "CTRL." In another sample of $N = 10$ NDs the temperature was probed by a ND inside the cell before and after picrotoxin administration. This sample is referred to as "+PICRO." Starting from this condition, a sample of $N = 8$ temperature variation repeated measurements was performed in a ND inside the cell before and after TTX and cadmium administration. This is referred to as "+PICRO+TTX+Cd."

The temperature variation ΔT detected by the NV sensor was evaluated through a direct fluorescence change measurement, as described before, the equation being

$$\Delta T = \frac{\Delta \bar{F}}{\text{slope} \cdot \partial D_{\text{gs}} / \partial T} \quad (7)$$

Every single measure of temperature change ΔT_i was affected by an uncertainty $\sigma(\Delta T_i)$. For its estimation, the error propagation of the variables that appear in Equation (7) has been carried out. In the following, the involved uncertainties are analyzed in detail.

The term $\Delta \bar{F}$ is the difference between the differential spectrum signal \bar{F} before and after the substance perfusion. The associated uncertainty is the sum in quadrature: $\sigma(\Delta \bar{F}) = \sqrt{[\sigma(\bar{F}_{\text{after}})]^2 + [\sigma(\bar{F}_{\text{before}})]^2}$. Where $\sigma(\bar{F})$

Table 2. Summary of temperature variation $\Delta T \pm \sigma \Delta T$ [°C] for the three (sample size, respectively, $N = 11$, $N = 10$, $N = 8$) independent groups.

$\Delta T \pm \sigma(\Delta T)$ [°C]		
CTRL	+PICRO	+PICRO+TTX+Cd
-0.08 ± 0.77	1.39 ± 0.76	0.18 ± 0.80
-0.27 ± 0.49	1.38 ± 1.02	0.14 ± 0.48
-0.17 ± 0.47	1.01 ± 0.90	-0.63 ± 0.29
-0.60 ± 1.23	0.65 ± 0.64	-1.46 ± 0.72
0.33 ± 0.33	1.73 ± 0.85	-0.76 ± 0.60
0.42 ± 0.88	1.04 ± 0.65	-0.92 ± 0.57
0.18 ± 0.59	1.12 ± 1.10	-0.20 ± 0.31
-0.07 ± 0.49	0.70 ± 1.06	-1.50 ± 0.77
0.29 ± 0.33	1.04 ± 0.49	
-0.47 ± 0.55	0.73 ± 0.57	
-0.01 ± 0.44		

Table 3. Summary of statistical parameters for the Welch's t -test.

CTRL versus +PICRO+TTX+Cd	
Welch's t value	7.63
Degree of freedom	14.15
Significance Welch's t test	2.21×10^{-6}
CTRL versus +PICRO	
Welch's t value	11.24
Degree of freedom	14.90
Significance Welch's t test	1.12×10^{-8}

is data standard deviation divided by the square root of repeated measurements (500 values in 60 s).

As well as the PL, the slope was also evaluated on every single measurement. The associated uncertainty $\sigma(\text{slope})$ was evaluated by the linear regression of the linear region differential spectrum.

The constant $\partial D_{gs}/\partial T$ was evaluated by a previous measurement, analyzing a sample of $N = 6$ NDs (Table 1) as described in the Section "Method to obtain $\partial D_{gs}/\partial T$ ". Unlike previous contributions, its associated uncertainty acts as a b type uncertainty, intervening only in the errors propagation on the average value estimate of each data set. The values ΔT_i and $\sigma(\Delta T_i)$ are shown in Table 2.

To prove the main result of this work it was necessary to demonstrate a significant statistical difference between the "+PICRO" and the "CTRL" sets. This can be formalized by evaluating the probability that ΔT_{+PICRO} and ΔT_{CTRL} belong to the same population, which is the starting null hypothesis. The Welch t -student test was performed for this purpose. The calculated values for the stochastic t variable, the population degree of freedom and the probability of satisfying the null hypothesis are shown in Table 3.

The test significance obtained allowed rejecting the initial null hypothesis. The two samples did not belong to the same population and therefore the increase in temperature, recorded following picrotoxin perfusion, was statistically significant. The same test was repeated to compare the "CTRL" and "+PICRO+TTX+Cd" sets in order to understand if the decrease in temperature recorded by the nanodiamonds following the TTX and Cd perfusion is statistically significant. As can be seen from Table 3, also in this case it is possible to reject the null hypothesis. The two samples did not belong to the same population and therefore the decrease in temperature was statistically significant.

All the statistical analysis was performed by using Wolfram Mathematica software.

Acknowledgements

The authors acknowledge Prof. E. Carbone for useful discussion and C. Franchino for cell preparation. This project (No. 20IND05) QADeT leading to this publication has received funding from the EMPIR program co-financed by the Participating States and from the European Union's Horizon 2020 research and innovation program. The project was further supported by PATHOS EU H2020 FET-OPEN Grant No. 828946 Horizon 2020, and European Regional Development Fund; OP RDE; Project CARAT (No. CZ.02.1.01/0.0/0.0/16_026/0008382), Compagnia di San Paolo, PROGETTO TRAPEZIO.

Conflict of Interest

The authors declare no conflict of interest.

Author Contributions

G.P. and G.T. contributed equally to this work. M.G., V.C., E.B., E.M., I.P.D., P.C., and P.T. planned the experiment. The main experimental work was equally realized by G.T. (for the biological part) and G.P. (optical one) with the direct help and supervision of E.B. and E.M. (for the optical one) in the laboratories directed by V.C. (biological one) and M.G. (optical one). The quantum sensing facility at INRIM was developed by E.M., E.B., and P.T. All the authors equally contributed to the discussion on experimental settings and on data analysis, as well as in writing the paper. P.C. and K.K. provided the nanodiamond samples.

Data Availability Statement

The data that support the findings of this study are available from the corresponding author upon reasonable request.

Keywords

intracellular nanoscale sensing, nanodiamonds, nitrogen-vacancy (NV) centers, ODMR

Received: May 30, 2022

Revised: June 28, 2022

Published online: July 25, 2022

- [1] C. Robert, I. Hue, S. McGraw, D. Gagné, M. A. Sirard, *Quantification of Cyclin B1 and P34cdc2 in Bovine Cumulus-Oocyte Complexes and Expression Mapping of Genes Involved in the Cell Cycle by Complementary DNA Microarrays*, Vol. 67, Sinauer Associates, Inc., Sunderland, MA, 2002, pp. 1456.
- [2] T. O'Leary, E. Marder, *Curr. Biol.* **2016**, 26, 2935.
- [3] L. Bui, M. I. Glavinović, *Cogn. Neurodyn.* **2014**, 8, 277.
- [4] D. G. Margineanu, E. Schoffeniels, *Proc. Natl. Acad. Sci. USA* **1977**, 74, 3810.
- [5] J. V. Howarth, J. M. Ritchie, D. Stagg, *Proc. R. Soc. London, Ser. B* **1979**, 205, 347.
- [6] A. C. L. De Lichtervelde, J. P. De Souza, M. Z. Bazant, *Phys. Rev. E* **2020**, 101, 22406.

- [7] J. Choi, H. Zhou, R. Landig, H. Y. Wu, X. Yu, S. E. von Stetina, G. Kucsko, S. E. Mango, D. J. Needleman, A. D. T. Samuel, P. C. Maurer, H. Park, M. D. Lukin, *Proc. Natl. Acad. Sci. USA* **2020**, *117*, 14636.
- [8] L. De Meis, L. A. Ketzner, R. M. Da Costa, I. R. De Andrade, M. Benchimol, *PLoS One* **2010**, *5*, e9439.
- [9] S. M. Thompson, L. M. Masukawa, D. A. Prince, *J. Neurosci.* **1985**, *5*, 817.
- [10] M. Volgushev, T. R. Vidyasagar, M. Chistiakova, U. T. Eysel, *Neuroscience* **2000**, *98*, 9.
- [11] J. C. F. Lee, J. C. Callaway, R. C. Foehring, *J. Neurophysiol.* **2005**, *93*, 2012.
- [12] M. E. Raichle, *Proc. Natl. Acad. Sci. USA* **1998**, *95*, 765.
- [13] M. Monti, L. Brandt, J. Ikomi-Kumm, H. Olsson, *Scand. J. Haematol.* **1986**, *36*, 353.
- [14] M. Ghavami, M. Rezaei, R. Ejtehad, M. Lotfi, M. A. Shokrgozar, B. Abd Emamy, J. Raush, M. Mahmoudi, *ACS Chem. Neurosci.* **2013**, *4*, 375.
- [15] P. Liang, Y. Xu, X. Zhang, C. Ding, R. Huang, Z. Zhang, J. Lv, X. Xie, Y. Chen, Y. Li, Y. Sun, Y. Bai, Z. Songyang, W. Ma, C. Zhou, J. Huang, *Protein Cell* **2015**, *6*, 363.
- [16] M. Fujiwara, S. Sun, A. Dohms, Y. Nishimura, K. Suto, Y. Takezawa, K. Oshimi, L. Zhao, N. Sadzak, Y. Umehara, Y. Teki, N. Komatsu, O. Benson, Y. Shikano, E. Kage-Nakada, *Sci. Adv.* **2020**, *6*, eaba9636.
- [17] J.-M. Yang, H. Yang, L. Lin, *ACS Nano* **2011**, *5*, 5067.
- [18] S. Kiyonaka, T. Kajimoto, R. Sakaguchi, D. Shinmi, M. Omatsu-Kanbe, H. Matsuura, H. Imamura, T. Yoshizaki, I. Hamachi, T. Morii, Y. Mori, *Nat. Methods* **2013**, *10*, 1232.
- [19] D. Chrétien, P. Béné, H. H. Ha, S. Keipert, R. El-Khoury, Y. T. Chang, M. Jastroch, H. T. Jacobs, P. Rustin, M. Rak, *PLoS Biol.* **2018**, *16*, e2003992.
- [20] G. Baffou, H. Rigneault, D. Marguet, L. Jullien, *Nat. Methods* **2014**, *11*, 899.
- [21] M. Suzuki, V. Zeeb, S. Arai, K. Oyama, S. Ishiwata, *Nat. Methods* **2015**, *12*, 802.
- [22] M. Suzuki, T. Plakhotnik, *Biophys. Rev.* **2020**, *12*, 593.
- [23] F. Vetrone, R. Naccache, A. Zamarrón, A. J. De La Fuente, F. Sanz-Rodríguez, L. M. Maestro, E. M. Rodríguez, D. Jaque, J. G. Sole, J. A. Capobianco, *ACS Nano* **2010**, *4*, 3254.
- [24] M. Li, T. Chen, J. J. Gooding, J. Liu, *ACS Sens.* **2019**, *4*, 1732.
- [25] S. W. Allison, G. T. Gillies, A. J. Rondinone, M. R. Cates, *Nanotechnology* **2003**, *14*, 859.
- [26] L. Guarina, C. Calorio, D. Gavello, E. Moreva, P. Traina, A. Battiato, S. Ditalia Tchernij, J. Forneris, M. Gai, F. Picollo, P. Olivero, M. Genovese, E. Carbone, A. Marcantoni, V. Carabelli, *Sci. Rep.* **2018**, *8*, 2221.
- [27] G. Petrini, E. Moreva, E. Bernardi, P. Traina, G. Tomagra, V. Carabelli, I. P. Degiovanni, M. Genovese, *Adv. Quantum Technol.* **2020**, *3*, 2000066.
- [28] T. Zhang, G. Pramanik, K. Zhang, M. Gulka, L. Wang, J. Jing, F. Xu, Z. Li, Q. Wei, P. Cigler, Z. Chu, *ACS Sens.* **2021**, *6*, 2077.
- [29] M. Fujiwara, Y. Shikano, *Nanotechnology* **2021**, *32*, 482002.
- [30] C. Bradac, S. F. Lim, H. C. Chang, I. Aharonovich, *Adv. Opt. Mater.* **2020**, *8*, 2000183.
- [31] I. V. Fedotov, M. A. Solotnikov, M. S. Pochechuev, O. I. Ivashkina, S. Y. Kilin, K. V. Anokhin, A. M. Zheltikov, *ACS Photonics* **2020**, *7*, 3353.
- [32] P. C. Tsai, C. P. Epperla, J. S. Huang, O. Y. Chen, C. C. Wu, H. C. Chang, *Angew. Chem., – Int. Ed.* **2017**, *56*, 3025.
- [33] W. Liu, M. N. A. Alam, Y. Liu, V. N. Agafonov, H. Qi, K. Koynov, V. A. Davydov, R. Uzbekov, U. Kaiser, T. Lasser, F. Jelezko, A. Ermakova, T. Weil, *Nano Lett.* **2022**, *22*, 2881.
- [34] K. Ambal, R. D. McMichael, *Rev. Sci. Instrum.* **2019**, *90*, 023907.
- [35] Y. Wu, T. Weil, *Adv. Sci.* **2022**, <https://doi.org/10.1002/advsc.202200059>.
- [36] M. Fujiwara, A. Dohms, K. Suto, Y. Nishimura, K. Oshimi, Y. Teki, K. Cai, O. Benson, Y. Shikano, *Phys. Rev. Res.* **2020**, *2*, 043415.
- [37] G. Kucsko, P. C. Maurer, N. Y. Yao, M. Kubo, H. J. Noh, P. K. Lo, H. Park, M. D. Lukin, *Nature* **2013**, *500*, 54.
- [38] D. A. Simpson, E. Morrisroe, J. M. McCoe, A. H. Lombard, D. C. Mendis, F. Treussart, L. T. Hall, S. Petrou, L. C. L. Hollenberg, *ACS Nano* **2017**, *11*, 12077.
- [39] V. Tseeb, M. Suzuki, K. Oyama, K. Iwai, S. Ishiwata, *HFSP J.* **2009**, *3*, 117.
- [40] S. K. R. Singam, M. Nesladek, E. Goovaerts, *Nanotechnology* **2020**, *31*, 105501.
- [41] K. Sasaki, Y. Monnai, S. Saijo, R. Fujita, H. Watanabe, J. Ishi-Hayase, K. M. Itoh, E. Abe, *Rev. Sci. Instrum.* **2016**, *87*, 053904.
- [42] Y. A. Huang, C. W. Kao, K. K. Liu, H. S. Huang, M. H. Chiang, C. R. Soo, H. C. Chang, T. W. Chiu, J. I. Chao, E. Hwang, *Sci. Rep.* **2014**, *4*, 1.
- [43] M. Papa, M. Segal, *Neuroscience* **1996**, *71*, 1005.
- [44] A. Marcantoni, M. S. Cerullo, P. Buxeda, G. Tomagra, M. Giustetto, G. Chiantia, V. Carabelli, E. Carbone, *J. Physiol.* **2020**, *598*, 2183.
- [45] D. Attwell, S. B. Laughlin, *J. Cereb. Blood Flow Metab.* **2001**, *21*, 1133.
- [46] B. E. Leonard, *Hum. Psychopharmacol. Clin. Exp.* **1993**, *8*, 294.
- [47] D. Gavello, C. Calorio, C. Franchino, F. Cesano, V. Carabelli, E. Carbone, A. Marcantoni, *Cereb. Cortex* **2018**, *28*, 433.
- [48] I. Russo, D. Gavello, E. Menna, D. Vandael, C. Veglia, N. Morello, I. Corradini, E. Focchi, A. Alfieri, C. Angelini, F. T. Bianchi, A. Morellato, A. Marcantoni, M. Sassoè-Pognetto, M. M. Ottaviani, L. Yekhelef, M. Giustetto, S. Taverna, V. Carabelli, M. Matteoli, E. Carbone, E. Turco, P. Defilippi, *Cereb. Cortex* **2019**, *29*, 91.
- [49] N. Fujiwara, H. Higashi, S. Nishi, K. Shimoji, S. Sugita, M. Yoshimura, *J. Physiol.* **1988**, *402*, 155.
- [50] E. Moreva, E. Bernardi, P. Traina, A. Soso, S. D. Tchernij, J. Forneris, F. Picollo, G. Brida, Z. Pastuović, I. P. Degiovanni, P. Olivero, M. Genovese, *Phys. Rev. Appl.* **2020**, *13*, 054057.
- [51] D. Gatto Monticone, K. Katamadze, P. Traina, E. Moreva, J. Forneris, I. Ruò-Berchera, P. Olivero, I. P. Degiovanni, G. Brida, M. Genovese, *Phys. Rev. Lett.* **2014**, *113*, 143602.
- [52] S. M. Smith, *Hum. Brain Mapp.* **2002**, *17*, 143.
- [53] V. M. Acosta, E. Bauch, M. P. Ledbetter, A. Waxman, L. S. Bouchard, D. Budker, *Phys. Rev. Lett.* **2010**, *104*, 070801.
- [54] X. D. Chen, C. H. Dong, F. W. Sun, C. L. Zou, J. M. Cui, Z. F. Han, G. C. Guo, *Appl. Phys. Lett.* **2011**, *99*, 161903.
- [55] K. Kvakova, M. Ondra, J. Schimer, M. Petrik, Z. Novy, H. Raabova, M. Hajdich, P. Cigler, *Adv. Funct. Mater.* **2022**, *32*, 2109960.
- [56] M. Capelli, A. H. Heffernan, T. Ohshima, H. Abe, J. Jeske, A. Hope, A. D. Greentree, P. Reineck, B. C. Gibson, *Carbon* **2019**, *143*, 714.
- [57] T. Rendler, J. Neburkova, O. Zemek, J. Kotek, A. Zappe, Z. Chu, P. Cigler, J. Wrachtrup, *Nat. Commun.* **2017**, *8*, 14701.